NANO LETTERS

pubs.acs.org/NanoLett Letter

Spontaneous Lithiation of Binary Oxides during Epitaxial Growth on $LiCoO_2$

Le Wang,*[,] Zhenzhong Yang,[] Widitha S. Samarakoon, Yadong Zhou, Mark E. Bowden, Hua Zhou, Jinhui Tao, Zihua Zhu, Nabajit Lahiri, Timothy C. Droubay, Zachary Lebens-Higgins, Xinmao Yin, Chi Sin Tang, Zhenxing Feng, Louis F. J. Piper, Andrew T. S. Wee, Scott A. Chambers, and Yingge Du*

Cite This: *Nano Lett.* 2022, 22, 5530−5537 Read Online

ACCESS | Metrics & More | Article Recommendations | Supporting Information

ABSTRACT: Epitaxial growth is a powerful tool for synthesizing heterostructures and integrating multiple functionalities. However, interfacial mixing can readily occur and significantly modify the properties of layered structures, particularly for those containing energy storage materials with smaller cations. Here, we show a two-step sequence involving the growth of an epitaxial $LiCoO_2$ cathode layer followed by the deposition of a binary transition metal oxide. Orientation-controlled epitaxial synthesis of the model solid-state-electrolyte Li_2WO_4 and anode material $Li_4Ti_5O_{12}$ occurs as WO_3 and TiO_2 nucleate and react with Li ions from the underlying cathode. We demonstrate that this lithiation-assisted epitaxy approach can be used for energy materials discovery and exploring different combinations of epitaxial interfaces that can serve as well-defined model systems for mechanistic studies of energy storage and conversion processes.

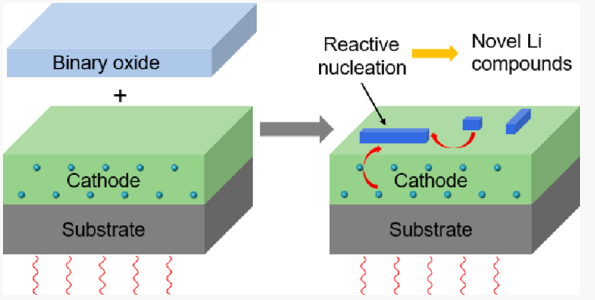

KEYWORDS: *$LiCoO_2$, Li-ions diffusion, surface reaction, thin films, energy materials*

Epitaxial growth is a powerful method for fabricating well-defined heterostructures of various kinds with tailored functionalities.[1] Successful implementation of heteroepitaxy for the preparation of multilayer structures such as superlattices usually relies on the ability to suppress the mixing of layers and thus fabricate abrupt interfaces,[2,3] as illustrated in Figure 1a. However, in many cases intermixing is unavoidable due to both thermodynamic and kinetic drivers and impacts the properties of interest.[4−7] Figure 1a can be also envisioned as a route to the vertical integration of a cathode material (film 1) with another electrolyte (film 2) in a prototypical solid-state lithium-ion battery (LIB), which is increasingly regarded as one of the most promising next-generation energy storage solutions. In this case, the interface is expected to be less abrupt due to the abundance and high mobility of Li ions. Studying atomic species exchange at the solid−solid interface has become one of the major topics for making progress in the development of solid-state LIBs.[8] However, it is still a big challenge in understanding how Li ions transport in different materials because of the ill-defined interfaces. Therefore, exploring the epitaxial integration of energy materials becomes very important, as well-defined interfaces offer an ideal testbed for fundamental studies of the performance and degradation mechanisms in solid-state LIBs.

$LiCoO_2$ with a layered structure is one of the most widely studied and employed cathode materials in LIBs.[9] It has been reported that the Li-ion diffusion energy barrier along the Li-containing planes is only 0.3 eV, whereas the Li-ion diffusion energy barrier along a vertical direction directly through the CoO_2 sheets is around 6.8 eV.[10] Thus, the Li-ion diffusion is usually two-dimensionally (2D) confined by the adjacent CoO_2 planes. Previous studies have shown that $LiCoO_2$ thin films can be epitaxially grown on $SrTiO_3$ (STO) by pulsed laser deposition (PLD), and the crystallographic orientation of $LiCoO_2$ strongly depends on that of STO.[11−14] Growing $LiCoO_2$ on (001)-oriented STO leads to $LiCoO_2$(104) and the Li-containing planes intersect the STO(001) surface by an angle of 54.7°.[14,15] Because of the 54.7° tilt of the Li-containing planes on the 4-fold symmetric substrate, twin boundaries (TBs) are observed in $LiCoO_2$/STO(001),[14,15] as depicted in Figure S1 and Figure 1c. Previous first principle calculations have shown that the Li-ion diffusion energy barrier (∼0.2 eV) along/across TBs is only ∼0.2 eV,[16,17] indicating that TBs could provide faster Li-ion diffusion channels.[18,19] Growing $LiCoO_2$ on (111)-oriented STO substrate leads to $LiCoO_2$(00l) and the Li-containing planes are parallel to the

Received: April 27, 2022
Revised: June 20, 2022
Published: June 30, 2022

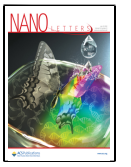

https://doi.org/10.1021/acs.nanolett.2c01701
Nano Lett. 2022, 22, 5530−5537

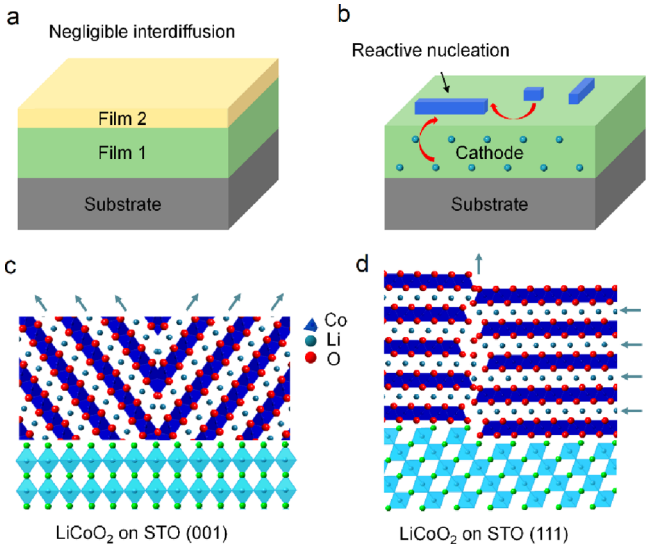

Figure 1. Conceptual illustration. (a) Schematic illustration of multistep epitaxial thin film growth with negligible interdiffusion. (b) Schematic illustration of the formation of a novel Li-containing phase resulting from Li out-diffusion when a low-density binary oxide is deposited on a cathode epitaxial base layer. Lattice models for (c) $LiCoO_2$ on STO(001) and (d) $LiCoO_2$ on STO(111), highlighting a twin boundary (TB) and an antiphase boundary (APB) in epitaxial $LiCoO_2$ thin films, respectively. The gray arrows denote the Li ion diffusion pathways in the two structures.

interface.[14] In this case, the dominant defects are antiphase boundaries (APBs), as illustrated in Figure S1 and Figure 1d. It has been proposed that APBs can function as viable mass-transfer channels that couple in-plane Li ion diffusion pathways.[20]

We show here that out-diffused Li ions from well-defined epitaxial $LiCoO_2$ cathode layers can be harnessed for the controlled synthesis of model energy-material heterostructures. The deposition process involves the reaction of Li ions from $LiCoO_2$ with the transition metal oxide (TMO) species such as WO_3 and TiO_2 as they nucleate. Highly oriented films of Li_2WO_4 and $Li_4Ti_5O_{12}$ spontaneously form in the process of lithiation-assisted epitaxy, as illustrated in Figure 1b. Our combined diffraction, microscopy, and spectroscopy studies correlate the resulting structures and morphologies with the presence of defects in the $LiCoO_2$ layers, the roles of which have previously been hypothesized but not yet established.

$LiCoO_2$ thin films of thickness 90 to 200 nm were grown on STO (001) and STO (111) single crystal substrates by PLD. During deposition, the substrates were heated to 600 °C and the growth oxygen pressure (PO_2) was 10 mTorr. After the growth of the $LiCoO_2$ cathode seed layer, the substrate temperature was held at 600 °C while PO_2 was raised to 100 mTorr for the deposition of the WO_3 or TiO_2 film. For comparison, one single layer of the WO_3 or TiO_2 film was directly grown on STO substrates under the same growth conditions.

A high-resolution X-ray diffraction (XRD) out-of-plane θ–2θ scan of a WO_3/STO(001) sample synthesized by PLD (black curve in Figure 2a) displays a single set of (00l) film peaks along with the STO substrate peaks, consistent with the nucleation of pseudocubic WO_3.[21,22] The vacant interstitial sites in the cubic WO_3 lattice allow for reversible intercalation and removal of small ions (e.g., H^+, Li^+, Na^+, and Ca^{2+}),[23,24] rendering this material useful in sensing and electrochromic devices. It is thus of interest to deposit WO_3 on $LiCoO_2$ to see if Li out-diffusion readily occurs. If Li diffusion can be completely suppressed, it is conceivable that $WO_3(001)$ would grow epitaxially on $LiCoO_2(104)$ as there is a structural match between the two materials. However, due to the high diffusivity of Li at elevated deposition temperature (e.g., 600 °C) and the high likelihood of reaction between WO_3 and Li, various reaction intermediates or final products may form. For example, substoichiometric Li ion insertion into the WO_3 lattice can produce lithium tungsten bronze Li_xWO_3 ($0 \leq x \leq 1$),[25] whereas a higher degree of lithiation could lead to cation-intercalated lithium tungstates ($Li_xWO_{3+x/2}$).[26−28] XRD out-of-plane θ–2θ scan (blue curve in Figure 2a) taken after the sequential deposition of ~120 nm $LiCoO_2$ and 30 nm of WO_3 at 600 °C on STO(001) displays a single Bragg peak that is clearly at a different angle than that of the WO_3 film and is located at a lower angle than that of the $LiCoO_2(104)$ diffraction peak. The XRD scan together with scanning transmission electron microscopy (STEM) data (Figure 2b–d) reveal that this material is phase pure Li_2WO_4 with the epitaxial orientations $Li_2WO_4(004) \parallel LiCoO_2(104) \parallel STO(001)$ and $Li_2WO_4[010] \parallel LiCoO_2[010] \parallel STO[110]$. The apparent reaction that occurs during WO_3 deposition at elevated temperatures is

$$2Li + 1/2O_2 + WO_3 \rightarrow Li_2WO_4 \quad (1)$$

We note that a control experiment consisting of WO_3 deposition on $LiCoO_2$/STO(001) at room temperature results only in a $LiCoO_2$ (104) diffraction peak (Figure S2), revealing that thermal energy is required to promote out-diffusion of Li to form crystalline Li_2WO_4.

Li_2WO_4 has a tetragonal structure ($a = b = 11.94$ Å, $c = 8.41$ Å)[29] in which Li atoms are distributed around the edge-sharing WO_6 octahedral network, as shown in Figure 2d. This oxide has been of interest for its use as a solid-state electrolyte.[30] Although its crystal structure has been readily elucidated by XRD, previous attempts to directly image the Li_2WO_4 lattice by TEM have been largely unsuccessful as Li_2WO_4 is electron beam sensitive due to the high mobility of Li under irradiation.[31] In Figure 2d, we show an atomically resolved high-angle annular dark-field STEM (HAADF-STEM) image of Li_2WO_4 viewed along the [010] direction with the corresponding structural model superimposed on top. The four adjacent bright features are columns of (high-Z) W. Epitaxial strain is likely to provide enhanced structural stability, allowing us to obtain atomically resolved images.

We also performed atomic force microscopy (AFM) for each film surface. As shown in the insets of Figure 2a, both $LiCoO_2$ and WO_3 thin films display flat surfaces with a root-mean square roughness of <1 nm over an area of 20 μm × 20 μm. In contrast, Li_2WO_4 predominately nucleates as elongated nanorods when deposited on $LiCoO_2(104)$/STO(001) whereas a small number of pyramid-shaped islands are also observed. A large-scale STEM image of $Li_2WO_4/LiCoO_2$/STO(001) shown in Figure 2b is consistent with our AFM studies. Thickness-dependent AFM studies (Figure 2e) reveal that Li_2WO_4 initially nucleates as nanoislands and that these subsequently align to form the elongated nanorods. We propose a model to correlate the preferred nucleation sites with the TBs of $LiCoO_2$. The large distance between the intersection of CoO_2 planes with the surface in $LiCoO_2(104)$ makes the diffusion of surface adatoms anisotropic. The TBs

https://doi.org/10.1021/acs.nanolett.2c01701
Nano Lett. 2022, 22, 5530−5537

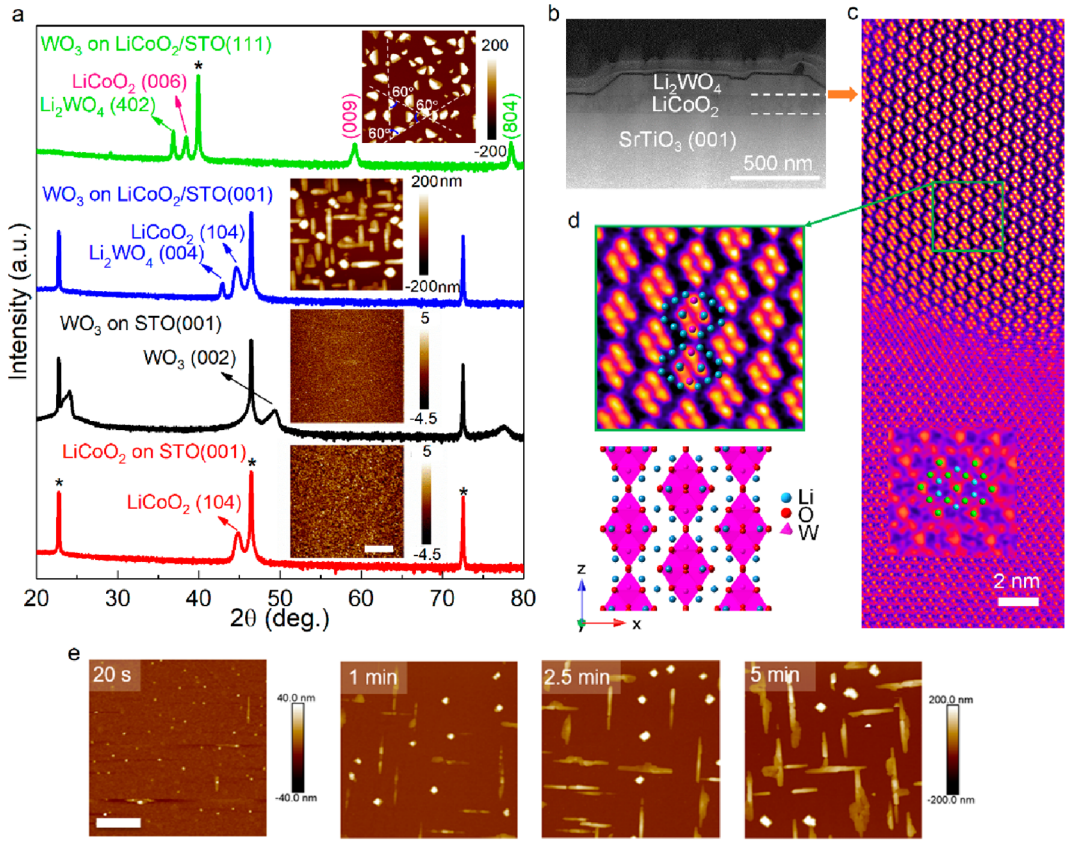

Figure 2. One archetypal example, Li_2WO_4 (from deposition of WO_3 on $LiCoO_2$). (a) X-ray diffraction $\theta-2\theta$ scans of $LiCoO_2$ on STO(001), WO_3 on STO(001), WO_3 on $LiCoO_2$/STO(001), and WO_3 on $LiCoO_2$/STO(111). The asterisks indicate the substrate Bragg peaks. The corresponding AFM images are shown in the insets. The lateral scale bar is 5 μm and the unit in all vertical scale bars is nm. (b) Cross-sectional STEM image of $Li_2WO_4/LiCoO_2$/STO(001) viewed along [110] direction in the STO substrate. The dashed lines indicate the interfaces. (c) High-resolution HAADF STEM image of the top $Li_2WO_4/LiCoO_2$ interface grown on STO(001), where the layered $LiCoO_2$ portion has transformed to spinel structure due to Li loss to the WO_3 layer. The spinel structure of $LiCo_2O_4$ (green spheres, Co; blue spheres, Li) is also overlaid for comparison. (d) HAADF STEM image of the Li_2WO_4 film overlapped with the crystal structure (top) and the bulk Li_2WO_4 structure viewed along [010] (bottom). (e) Surface morphological evolution of PLD-grown WO_3 on $LiCoO_2$/STO(001) at a substrate temperature of 600 °C. All AFM images have the same scale bar (5 μm). The number of WO_3 moieties incident on the surfaces is linearly proportional to deposition time in our PLD setup at fixed growth conditions. The deposition time was varied from 20 s to 5 min from left to right.

thus interrupt the diffusion path, rendering these defects as likely nucleation sites. The initial nuclei are highly localized nanodots and continued deposition leads to the merging of individual nanodots to form elongated nanorods on top of TBs. Pyramid-shaped islands are presumably formed because of random nucleation on terraces sufficiently large that adatoms cannot reach the preferred TBs sites before condensing.

The Li-containing planes in $LiCoO_2$ can be oriented parallel to the surface by depositing on STO(111), as shown in Figure 1d. In contrast to $LiCoO_2$/STO(001), the dominant defects for $LiCoO_2$/STO(111) are APBs. Therefore, deposition of WO_3 on $LiCoO_2$/STO(111) may allow us to determine if Li can participate in the subsequent reactions by diffusing through the APBs.[20] As shown in Figure 2a, XRD $\theta-2\theta$ scan for WO_3 on $LiCoO_2$/STO(111) deposited at 600 °C (green curve) confirms that phase-pure Li_2WO_4(201) forms. Moreover, AFM measurements indicate that the film morphology consists of isolated islands with an isosceles triangular base. The longest edges of the base triangles are oriented along the ⟨110⟩ directions of STO as labeled in the inset of Figure 2a, indicating 6-fold symmetry. The formation of quasi randomly distributed Li_2WO_4 islands across the surface strongly suggests that the APBs are viable pathways for Li out-diffusion.

We have shown that Li_2WO_4 nucleation and growth is strongly mediated by defects in both $LiCoO_2$ orientations, but the roles these defects play are different for the two orientations. The TBs in $LiCoO_2$/STO(001) act as anchoring sites for nucleation, whereas the APBs in $LiCoO_2$/STO(111) serve as channels for Li diffusion. $LiCoO_2$ layers go through a delithiation process in both cases, but the impact on their crystal structures is different. For the case of $LiCoO_2$/STO(001), our data suggest that highly localized delithiation occurs directly beneath the Li_2WO_4 islands, as illustrated in Figure 3a. Part of the $LiCoO_2$ beneath the Li_2WO_4 islands shows a clear phase transition from the layered $LiCoO_2$ structure to a spinel $LiCo_2O_4$ structure (Figure 2c and Figure 3c), indicative of significant lithium loss.[14,32,33] APBs in $LiCoO_2$/STO(111) allow for redistribution of the remaining Li among different layers (as indicated by arrows in Figure 3b), effectively mitigating highly localized delithiation. As a result, the layered structure of $LiCoO_2$/STO(111) could be largely preserved after the growth of Li_2WO_4 islands (Figure 3d and Figure S3).

https://doi.org/10.1021/acs.nanolett.2c01701
Nano Lett. 2022, 22, 5530−5537

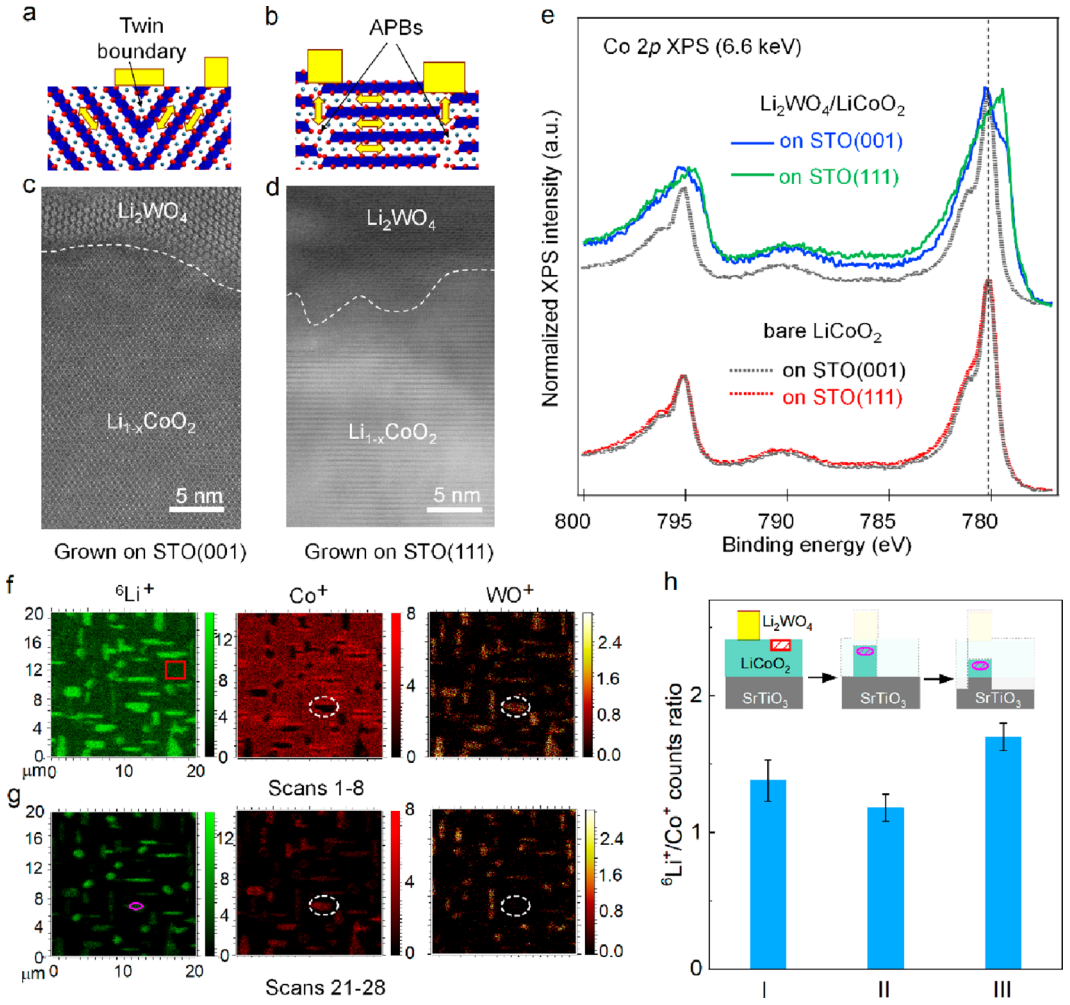

Figure 3. Impact on the structures of the cathode seed layer due to Li out-diffusion. (a,b) Schematic illustration of the connectivity between the nanostructures of $Li_2WO_4/LiCoO_2$ on STO(001) (a) and STO(111) (b). Yellow boxes denote Li_2WO_4 islands. Yellow arrows denote the Li ion diffusion pathways. (c,d) Cross-sectional STEM images of the $Li_2WO_4/LiCoO_2$ interface grown on STO(001) (c) and STO(111) (d) viewed along the [110] substrate orientation. The white dashed lines denote the interfaces. (e) Co 2*p* HAXPES of $LiCoO_2$ films before (bare $LiCoO_2$) and after covered by Li_2WO_4 islands. The black dash line is the guideline for peak position. For comparison, we overlay the Co 2p spectrum of bare $LiCoO_2$/STO(001) (dashed gray) on the Co 2p spectra of $Li_2WO_4/LiCoO_2$ samples. (f,g) ToF-SIMS images of $^6Li^+$, Co^+, and WO^+ for $Li_2WO_4/LiCoO_2$ on STO(001) summing over scans 1−8 (f) and 21−28 (g). The area marked by the red square in (f) corresponds to region I in the inset in (h), and this region was not covered by a Li_2WO_4 island. The island marked by the purple circle in (g) corresponds to region II (and region III at scans 29−37, not shown here) in the inset in (h). White dashed circles clearly show that a WO^+ signal was detected in scans 1−8 (f) but not in scans 21−28 (g), suggesting that the labeled Li_2WO_4 island has been sputtered away by the time scans 21−28 were collected. (h) $^6Li^+/Co^+$ counts ratio for $Li_2WO_4/LiCoO_2$ on STO(001) as a function of the sputter region. The error bars are based on the statistical analysis for multiple Li_2WO_4 islands. Schematic illustrations of the corresponding sputter region are shown on the top as the insets.

As only part of the $LiCoO_2$ seed layer is covered by Li_2WO_4 islands, Co signal can be still detected by X-ray photoelectron spectroscopy (XPS) measurements. At 6.6 keV, hard X-ray photoelectron spectroscopy (HAXPES) has an effective probing depth of ∼20 nm. Figure 3e compares HAXPES Co 2p spectra before and after the formation of Li_2WO_4 islands to probe the changes in Co valence. Li_2WO_4 islands can effectively block Co signals underneath, thus the contributions of Co signals are from $LiCoO_2$ regions not covered by Li_2WO_4. After the formation of Li_2WO_4 islands, Co 2p core levels are broader than that of $LiCoO_2$ and have contributions from both higher and lower binding energy sides, reflecting the coexistence of multiple valence states. In the reversible range, the delithiation of $LiCoO_2$ to form Li_xCoO_2 ($0.5 < x < 1$) is expected to oxidize Co above 3+. However, it is widely known that Li_xCoO_2 becomes increasingly unstable as x decreases, and releases oxygen at elevated temperatures, leading to reduce Co below 3+.[34,35] In addition, over delithiation can lead to the reduction of Co^{3+} as a result of spinel Co_3O_4 or rock-salt CoO formation.[14,35] $LiCoO_2$ regions not covered by Li_2WO_4 islands grown on STO(001) experience less Li loss as illustrated in Figure 3a and thus are expected to have better thermal stability. On the other hand, $LiCoO_2$ regions not covered by Li_2WO_4 islands readily contribute Li during the formation of Li_2WO_4 when growing on STO(111) (Figure 3b), which is more susceptible to reduce Co due to oxygen release at high temperature. As a result, the Co 2p spectrum of the $Li_2WO_4/LiCoO_2$/STO(111) sample shows a more pronounced change.

To visualize the lithium concentration change in different regions, three-dimensional (3D) time-of-flight secondary ion mass spectrometry (ToF-SIMS) imaging was conducted, and 2D images obtained at different depths were used to analyze

https://doi.org/10.1021/acs.nanolett.2c01701
Nano Lett. 2022, 22, 5530−5537

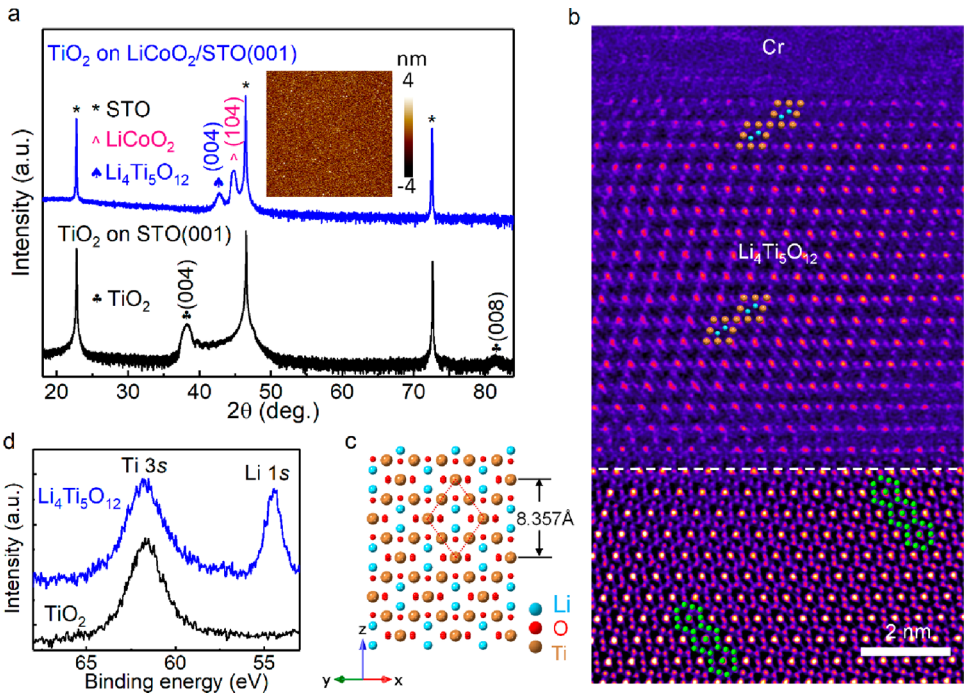

Figure 4. Deposition of TiO_2 on $LiCoO_2$/STO(001) leads to the formation of epitaxial $Li_4Ti_5O_{12}$. (a) X-ray diffraction θ–2θ scan for epitaxial TiO_2 on STO(001) and TiO_2 on $LiCoO_2$/STO(001). The AFM image for the latter is shown in the inset. The scale bar is 5 μm. (b) HAADF STEM image for the $Li_4Ti_5O_{12}/LiCoO_2$ interface with the $Li_4Ti_5O_{12}$ crystal structure overlapped with the image. The white dashed line denotes the interface. It should be noted that the $LiCoO_2$ region has clearly transformed to spinel structure after overdelithiation. The spinel structure of Co_3O_4 (green spheres, Co) is also overlaid for comparison. (c) The bulk $Li_4Ti_5O_{12}$ structure viewed along [110]. (d) Ti 3s XPS for the TiO_2 and $Li_4Ti_5O_{12}$ films. The Li 1s peak is clearly seen in the $Li_4Ti_5O_{12}$ spectrum.

compositional change. Figure 3f,g shows representative images for three positive ions ($^6Li^+$, Co^+, and WO^+) taken from the $Li_2WO_4/LiCoO_2$/STO(001) sample, displayed for scans 1–8 and 21–28. These 2D images reveal that the sample surface is not flat, and the specific features are consistent with AFM results (Figure 2a). Co^+ and WO^+ originate from the $LiCoO_2$ layer and Li_2WO_4 islands, respectively. As shown in Figure 3f, a WO^+ signal can be clearly seen in the region marked by the white dashed circle at scans 1–8. No Co+ signal was detected in this region, indicating that this island is Li_2WO_4. The WO^+ signal is gone in scans 21–28 (Figure 3g) whereas the Co^+ signal appears, suggesting that the Li_2WO_4 island has been sputtered away and the underlying $LiCoO_2$ layer is being imaged. On the basis of this analysis, the regions marked by the red square in Figure 3f and the purple circle in Figure 3g were chosen as region I and region II/region III in the inset in Figure 3h, respectively. Figure 3h summarizes the $^6Li^+/Co^+$ counts ratio as a function of the sputter region. When moving from region I (not covered by an Li_2WO_4 island) to region II (covered by an Li_2WO_4 island), the $^6Li^+/Co^+$ counts ratio drops, consistent with the fact of more Li loss occurs in region II because the delithiation process occurred in the cathode layer. The $^6Li^+/Co^+$ counts ratio increases when moving from region II to region III (same lateral location as region II but at a greater sputter depth), indicating that there was less Li loss in region III (close to the bottom interface) compared to region II. Furthermore, the $^6Li^+/Co^+$ counts ratio in region III is higher than that in region I, suggesting that some Li ions in region I also diffused away to form Li_2WO_4 due to surface diffusion at elevated temperature during the growth process.

The lithiation-assisted epitaxy approach described in Figure 1b can be readily extended to other materials systems, as seen in Figure 4 and Figure S4. Here we describe another archetypal example, $Li_4Ti_5O_{12}$, a known anode material used in LIBs,[36−39] formed by depositing TiO_2 onto $LiCoO_2$/STO(001) (Figure 4). The overall chemical reaction describing the interaction of Li with TiO_2 in the presence of excess oxygen is

$$4Li + O_2 + 5TiO_2 \rightarrow Li_4Ti_5O_{12} \quad (2)$$

Out-diffused Li from $LiCoO_2$ reacts with arriving TiO_2 species to form $Li_4Ti_5O_{12}$. XRD θ–2θ scan for a pure TiO_2 thin film grown directly on STO (001) (Figure 4a) shows two diffraction peaks, assigned as anatase TiO_2 (a-TiO_2) (004) and (008), consistent with previous reports.[40−42] In comparison, deposition of TiO_2 on top of $LiCoO_2$ leads to different peaks assigned to the (104) reflection of $LiCoO_2$ and the (004) reflection of $Li_4Ti_5O_{12}$. Bulk $Li_4Ti_5O_{12}$ exhibits a spinel structure with the lattice parameter of 8.357 Å (Figure 4c), matching what is estimated from our XRD measurement (8.445 Å). Figure 4b shows a HAADF STEM image of the $Li_4Ti_5O_{12}/LiCoO_2$ interface with the $Li_4Ti_5O_{12}$ lattice model overlaid on the image. The different contrast for Ti atoms results from different packing densities in the two kinds of Ti-containing columns in this structure.[36] Moreover, due to overdelithiation in the cathode layer, $LiCoO_2$ changes from the layered structure to the spinel Co_3O_4 structure. The Ti valence was analyzed using XPS and X-ray absorption spectroscopy (XAS). Figure 4d and Figure S5a show Ti 3s and Ti 2p XPS core-level spectra for a-TiO_2 and $Li_4Ti_5O_{12}$, respectively. No changes in peak shape and peak position are observed for Ti 3s and Ti 2p, confirming that the oxidation state for Ti is 4+ for both a-TiO_2 and $Li_4Ti_5O_{12}$. An additional peak appears at ~54.4 eV in the $Li_4Ti_5O_{12}$ spectrum and is assigned to Li 1s.[43,44] Figure S5b displays the normalized Ti L edge XAS

https://doi.org/10.1021/acs.nanolett.2c01701
Nano Lett. 2022, 22, 5530−5537

spectra of these two samples collected at room temperature. These spectra are in good agreement with that reported in the literature,[45,46] further confirming the chemical composition of *a*-TiO_2 and $Li_4Ti_5O_{12}$. In contrast to $Li_2WO_4/Li_{1-\delta}CoO_2$ (Figure 3e), no Co 2p signal was observed in the conventional XPS survey scan for $Li_4Ti_5O_{12}/Li_{1-\delta}CoO_2$ (Figure S6), indicating that the $Li_{1-\delta}CoO_2$ cathode seed layer was entirely covered by $Li_4Ti_5O_{12}$. This result is consistent with the flat surface revealed by AFM measurement (inset of Figure 4a). We note that many factors (such as the defects in the cathode seed layer, the binary transition metal oxide, and the growth temperature) affect the morphology of the resultant films. When fixed the defect type in the cathode layer and the growth temperature for depositing the binary oxide layer, the difference in the morphology of the resultant films is governed by the diffusion kinetics of different species during the nucleation and growth process. It has been reported that when WO_3 is evaporated, the majority species in the gas phase are stoichiometric W_3O_9 (or $(WO_3)_3$) clusters, also known as van der Waals complexes.[47,48] In contrast to other transition-metal oxides (such as TiO_2 and Fe_2O_3), these stoichiometric neutral $(WO_3)_3$ clusters have been shown to exhibit extremely weak interactions with O_2 and oxide support,[49] leading to a low diffusion barrier and long diffusion length that are favorable for Li_2WO_4 island growth. Thus, Li_2WO_4 on $LiCoO_2$/STO(001) have rodlike shape surface (Figure 2a), while $Li_4Ti_5O_{12}$ and $Li_{0.5}Fe_{1.5}O_{4-\delta}$ on $LiCoO_2$/STO(001) show smooth filmlike surface (Figure 4a and Figure S4a).

In summary, our study shows that the out-diffused Li ions from the cathode seed layers can react with the arriving species on the surface to form novel solid state energy materials during epitaxial growth. The examples we present are $WO_3/LiCoO_2 \rightarrow Li_2WO_4$ (a solid-state electrolyte) and $TiO_2/LiCoO_2 \rightarrow Li_4Ti_5O_{12}$ (an anode) with controlled structures and orientations. Additionally, we argue that this approach can be extended to other TMOs such as MoO_3 and Fe_2O_3 (as shown in Figure S4). We note that the phenomena we observed here can be compared to reactive solid-phase and solid−liquid phase epitaxy,[50−54] where small ions (e.g., Li^+ and Na^+) can be introduced to epitaxial films after the growth. Our work/approach involves the growth of epitaxial, reactive cathode layers first, which allows us to evaluate the critical roles of defects in regulating the subsequent epilayer composition, structure, orientation, and morphology, all of which are of vital importance in the design of functional materials and energy storage devices. This novel form of heteroepitaxy can mitigate challenges in synthesizing electrochemically active materials and rationally designed interfaces. First, the upper limit of available Li for the overlayer is determined by the thickness of the Li-containing cathode seed layer, and the degree of Li out-diffusion can be controlled by adjusting the growth temperature for the binary TMOs, thereby yielding access to useful reaction intermediates and/or metastable phases hidden in uncharted territory. Second, the structure and phase evolution as a function of lithiation in the overlayer yields a high-throughput testbed for energy materials discovery. Furthermore, the insights gained here should provide a better understanding of how Li-ions transport in different materials and may assist in designing structures, interfaces, and devices (such as $Au/Li_2WO_4/LiCoO_2$ and $Li_4Ti_5O_{12}/Li_2WO_4/LiCoO_2$) that are of pertinent interest to solid-state ionics and LIBs.

■ ASSOCIATED CONTENT

Supporting Information

The Supporting Information is available free of charge at https://pubs.acs.org/doi/10.1021/acs.nanolett.2c01701.

Methods; HAADF-STEM images; XRD and AFM for a WO_3 film grown on $LiCoO_2$/STO(001) at room temperature; cross-sectional STEM images of the $Li_2WO_4/LiCoO_2$ interface grown on STO(111); generality of the lithiation-assisted epitaxy approach to other materials systems; Ti 2p XPS and Ti *L*-edge XAS; survey XPS scans (PDF)

■ AUTHOR INFORMATION

Corresponding Authors

Le Wang − *Physical and Computational Sciences Directorate, Pacific Northwest National Laboratory, Richland, Washington 99354, United States;* orcid.org/0000-0002-7730-9482; Email: le.wang@pnnl.gov

Yingge Du − *Physical and Computational Sciences Directorate, Pacific Northwest National Laboratory, Richland, Washington 99354, United States;* orcid.org/0000-0001-9680-1950; Email: yingge.du@pnnl.gov

Authors

Zhenzhong Yang − *Physical and Computational Sciences Directorate, Pacific Northwest National Laboratory, Richland, Washington 99354, United States; Key Laboratory of Polar Materials and Devices (MOE) and Department of Electronics, East China Normal University, Shanghai 200062, China*

Widitha S. Samarakoon − *Physical and Computational Sciences Directorate, Pacific Northwest National Laboratory, Richland, Washington 99354, United States; School of Chemical, Biological, and Environmental Engineering, Oregon State University, Corvallis, Oregon 97331, United States*

Yadong Zhou − *Environmental Molecular Sciences Laboratory, Pacific Northwest National Laboratory, Richland, Washington 99352, United States; Key Laboratory of Geographic Information Science of the Ministry of Education, School of Geographic Sciences, East China Normal University, Minhang District, Shanghai 200241, China*

Mark E. Bowden − *Environmental Molecular Sciences Laboratory, Pacific Northwest National Laboratory, Richland, Washington 99352, United States;* orcid.org/0000-0003-3812-3340

Hua Zhou − *Advanced Photon Source, Argonne National Laboratory, Lemont, Illinois 60439, United States*

Jinhui Tao − *Physical and Computational Sciences Directorate, Pacific Northwest National Laboratory, Richland, Washington 99354, United States;* orcid.org/0000-0002-1156-9396

Zihua Zhu − *Environmental Molecular Sciences Laboratory, Pacific Northwest National Laboratory, Richland, Washington 99352, United States;* orcid.org/0000-0001-5770-8462

Nabajit Lahiri − *Physical and Computational Sciences Directorate, Pacific Northwest National Laboratory, Richland, Washington 99354, United States*

Timothy C. Droubay − *Physical and Computational Sciences Directorate, Pacific Northwest National Laboratory, Richland, Washington 99354, United States*

https://doi.org/10.1021/acs.nanolett.2c01701
Nano Lett. 2022, 22, 5530−5537

Zachary Lebens-Higgins − *Physics, Applied Physics, and Astronomy, Binghamton University, Binghamton, New York 13902, United States*

Xinmao Yin − *Physics Department, Shanghai Key Laboratory of High Temperature Superconductors, Shanghai University, Shanghai 200444, China;* orcid.org/0000-0002-8246-4444

Chi Sin Tang − *Institute of Materials Research and Engineering, A*STAR (Agency for Science, Technology and Research), Singapore 138634, Singapore; Singapore Synchrotron Light Source (SSLS), National University of Singapore, Singapore 117603, Singapore;* orcid.org/0000-0002-2414-7192

Zhenxing Feng − *School of Chemical, Biological, and Environmental Engineering, Oregon State University, Corvallis, Oregon 97331, United States;* orcid.org/0000-0001-7598-5076

Louis F. J. Piper − *Physics, Applied Physics, and Astronomy, Binghamton University, Binghamton, New York 13902, United States; WMG, The University of Warwick, Coventry CV4 7AL, United Kingdom;* orcid.org/0000-0002-3421-3210

Andrew T. S. Wee − *Department of Physics, Faculty of Science, National University of Singapore, Singapore 117551, Singapore;* orcid.org/0000-0002-5828-4312

Scott A. Chambers − *Physical and Computational Sciences Directorate, Pacific Northwest National Laboratory, Richland, Washington 99354, United States;* orcid.org/0000-0002-5415-043X

Complete contact information is available at: https://pubs.acs.org/10.1021/acs.nanolett.2c01701

Author Contributions

●L.W. and Z.Y. contributed equally.

Notes

The authors declare no competing financial interest.

■ ACKNOWLEDGMENTS

The work was supported by the U.S. Department of Energy (DOE), Office of Science, Office of Basic Energy Sciences (BES), Early Career Research Program under Award No. 68278. XPS and X-ray diffraction studies were supported by U.S. DOE BES Materials Science and Engineering Division under Award No. 10122. W.S.S. acknowledges the support from PNNL-OSU Distinguished Graduate Research Fellowship. Z.F. acknowledges the support from National Science Foundation under contract no. CBET-1949870 and CBET-2016192. This research used resources of APS, a U.S. DOE Office of Science User Facility operated by Argonne National Laboratory under contract DE-AC02-06CH11357. We thank Dr. Tiffany Kaspar for valuable discussions and thank the Diamond Light Source and Singapore Synchrotron Light Source for providing the facilities support. A portion of the work was performed at the W. R. Wiley Environmental Molecular Sciences Laboratory, a DOE User Facility sponsored by the Office of Biological and Environmental Research. PNNL is a multiprogram national laboratory operated for DOE by Battelle.

■ REFERENCES

(1) Ramesh, R.; Schlom, D. G. Creating emergent phenomena in oxide superlattices. *Nat. Rev. Mater.* **2019**, *4*, 257−268.

(2) Boschker, H.; Harada, T.; Asaba, T.; Ashoori, R.; Boris, A.; Hilgenkamp, H.; Hughes, C.; Holtz, M.; Li, L.; Muller, D. Ferromagnetism and conductivity in atomically thin $SrRuO_3$. *Phys. Rev. X* **2019**, *9* (1), 011027.

(3) Wang, L.; Yang, Z.; Bowden, M. E.; Freeland, J. W.; Sushko, P. V.; Spurgeon, S. R.; Matthews, B.; Samarakoon, W. S.; Zhou, H.; Feng, Z.; Engelhard, M. H.; Du, Y.; Chambers, S. A. Hole-Trapping-Induced Stabilization of Ni^{4+} in $SrNiO_3/LaFeO_3$ Superlattices. *Adv. Mater.* **2020**, *32* (45), 2005003.

(4) Nakagawa, N.; Hwang, H. Y.; Muller, D. A. Why some interfaces cannot be sharp. *Nat. Mater.* **2006**, *5* (3), 204−209.

(5) Willmott, P. R.; Pauli, S. A.; Herger, R.; Schleputz, C. M.; Martoccia, D.; Patterson, B. D.; Delley, B.; Clarke, R.; Kumah, D.; Cionca, C.; Yacoby, Y. Structural basis for the conducting interface between $LaAlO_3$ and $SrTiO_3$. *Phys. Rev. Lett.* **2007**, *99* (15), 155502.

(6) Chambers, S.A.; Engelhard, M.H.; Shutthanandan, V.; Zhu, Z.; Droubay, T.C.; Qiao, L.; Sushko, P.V.; Feng, T.; Lee, H.D.; Gustafsson, T.; Garfunkel, E.; Shah, A.B.; Zuo, J.-M.; Ramasse, Q.M. Instability, intermixing and electronic structure at the epitaxial $LaAlO_3/SrTiO_3$ (001) heterojunction. *Surf. Sci. Rep.* **2010**, *65* (10−12), 317−352.

(7) Spurgeon, S. R.; Sushko, P. V.; Chambers, S. A.; Comes, R. B. Dynamic interface rearrangement in $LaFeO_3$/n-$SrTiO_3$ heterojunctions. *Phys. Rev. Mater.* **2017**, *1* (6), 063401.

(8) Banerjee, A.; Wang, X.; Fang, C.; Wu, E. A.; Meng, Y. S. Interfaces and interphases in all-solid-state batteries with inorganic solid electrolytes. *Chem. Rev.* **2020**, *120* (14), 6878−6933.

(9) Lyu, Y.; Wu, X.; Wang, K.; Feng, Z.; Cheng, T.; Liu, Y.; Wang, M.; Chen, R.; Xu, L.; Zhou, J.; Lu, Y.; Guo, B. An Overview on the Advances of $LiCoO_2$ Cathodes for Lithium-Ion Batteries. *Adv. Energy Mater.* **2021**, *11* (2), 2000982.

(10) Van der Ven, A.; Ceder, G. Lithium diffusion mechanisms in layered intercalation compounds. *J. Power Sources* **2001**, *97*, 529−531.

(11) Nishio, K.; Ohnishi, T.; Akatsuka, K.; Takada, K. Crystal orientation of epitaxial $LiCoO_2$ films grown on $SrTiO_3$ substrates. *J. Power Sources* **2014**, *247*, 687−691.

(12) Takeuchi, S.; Tan, H.; Bharathi, K. K.; Stafford, G. R.; Shin, J.; Yasui, S.; Takeuchi, I.; Bendersky, L. A. Epitaxial $LiCoO_2$ films as a model system for fundamental electrochemical studies of positive electrodes. *ACS Appl. Mater. Interfaces* **2015**, *7* (15), 7901−7911.

(13) Li, Z.; Yasui, S.; Takeuchi, S.; Creuziger, A.; Maruyama, S.; Herzing, A.; Takeuchi, I.; Bendersky, L. Structural study of epitaxial LiCoO2 films grown by pulsed laser deposition on single crystal SrTiO3 substrates. *Thin Solid Films* **2016**, *612*, 472−482.

(14) Yang, Z.; Ong, P. V.; He, Y.; Wang, L.; Bowden, M. E.; Xu, W.; Droubay, T. C.; Wang, C.; Sushko, P. V.; Du, Y. Direct visualization of li dendrite effect on licoo2 cathode by in situ tem. *Small* **2018**, *14* (52), 1803108.

(15) Qin, C.; Wang, L.; Yan, P.; Du, Y.; Sui, M. $LiCoO_2$ Epitaxial Film Enabling Precise Analysis of Interfacial Degradations. *Chin. Phys. Lett.* **2021**, *38* (6), 068202.

(16) Moriwake, H.; Kuwabara, A.; Fisher, C. A.; Huang, R.; Hitosugi, T.; Ikuhara, Y. H.; Oki, H.; Ikuhara, Y. First-principles calculations of lithium-ion migration at a coherent grain boundary in a cathode material, $LiCoO_2$. *Adv. Mater.* **2013**, *25* (4), 618−622.

(17) Zhang, F.; Dong, J.; Yi, D.; Xia, J.; Lu, Z.; Yang, Y.; Wang, X. Archimedean polyhedron $LiCoO_2$ for ultrafast rechargeable Li-ion batteries. *Chem. Eng. J.* **2021**, *423*, 130122.

(18) Nie, A.; Gan, L.-Y.; Cheng, Y.; Li, Q.; Yuan, Y.; Mashayek, F.; Wang, H.; Klie, R.; Schwingenschlogl, U.; Shahbazian-Yassar, R. Twin boundary-assisted lithium ion transport. *Nano Lett.* **2015**, *15* (1), 610−615.

(19) Wang, R.; Chen, X.; Huang, Z.; Yang, J.; Liu, F.; Chu, M.; Liu, T.; Wang, C.; Zhu, W.; Li, S. Twin boundary defect engineering improves lithium-ion diffusion for fast-charging spinel cathode materials. *Nat. Commun.* **2021**, *12* (1), 1−10.

(20) Ong, P.-V.; Yang, Z.; Sushko, P. V.; Du, Y. Formation, Structural Variety, and Impact of Antiphase Boundaries on Li

Diffusion in $LiCoO_2$ Thin-Film Cathodes. *J. Phys. Chem. Lett.* **2018**, *9* (18), 5515−5520.
(21) Du, Y.; Gu, M.; Varga, T.; Wang, C.; Bowden, M. E.; Chambers, S. A. Strain accommodation by facile WO_6 octahedral distortion and tilting during WO3 heteroepitaxy on $SrTiO_3$ (001). *ACS Appl. Mater. Interfaces* **2014**, *6* (16), 14253−14258.
(22) Yang, J.-t.; Ma, C.; Ge, C.; Zhang, Q.-h.; Du, J.-y.; Li, J.-k.; Huang, H.-y.; He, M.; Wang, C.; Meng, S.; Gu, L.; Lu, H.-b.; Yang, G.-z.; Jin, K.-j. Effects of line defects on the electronic and optical properties of strain-engineered WO_3 thin films. *J. Mater. Chem. C* **2017**, *5* (45), 11694−11699.
(23) He, Y.; Gu, M.; Xiao, H.; Luo, L.; Shao, Y.; Gao, F.; Du, Y.; Mao, S. X.; Wang, C. Atomistic conversion reaction mechanism of WO_3 in secondary ion batteries of Li, Na, and Ca. *Angew. Chem., Int. Ed.* **2016**, *55* (21), 6244−6247.
(24) Wang, M.; Shen, S.; Ni, J.; Lu, N.; Li, Z.; Li, H.-B.; Yang, S.; Chen, T.; Guo, J.; Wang, Y.; Xiang, H.; Yu, P. Electric-Field-Controlled Phase Transformation in WO_3 Thin Films through Hydrogen Evolution. *Adv. Mater.* **2017**, *29* (46), 1703628.
(25) Hjelm, A.; Granqvist, C. G.; Wills, J. M. Electronic structure and optical properties of WO_3, $LiWO_3$, $NaWO_3$, and HWO_3. *Phys. Rev. B* **1996**, *54* (4), 2436.
(26) Nassau, K.; Glass, A.; Grasso, M.; Olson, D. Rapidly quenched tungstate and molybdate composition containing lithium: glass formation and ionic conductivity. *J. Electrochem. Soc.* **1980**, *127* (12), 2743.
(27) Yu, A.; Kumagai, N.; Liu, Z.; Lee, J. Y. Electrochemical lithium intercalation into WO_3 and lithium tungstates $Li_xWO_{3+x/2}$ of various structures. *J. Solid State Electrochem* **1998**, *2* (6), 394−400.
(28) Hu, Z.; Xiao, X.; Jin, H.; Li, T.; Chen, M.; Liang, Z.; Guo, Z.; Li, J.; Wan, J.; Huang, L.; Zhang, Y.; Feng, G.; Zhou, J. Rapid mass production of two-dimensional metal oxides and hydroxides via the molten salts method. *Nat. Commun.* **2017**, *8* (1), 1−9.
(29) Pistorius, C. W. Phase behavior of Li_2WO_4 at high pressures and temperatures. *J. Solid State Chem.* **1975**, *13* (4), 325−329.
(30) Yahaya, A.; Ibrahim, Z.; Arof, A. Thermal, electrical and structural properties of Li_2WO_4. *J. Alloys Compd.* **1996**, *241* (1−2), 148−152.
(31) Meng, F.; Guo, H.; Wang, Z.; Yan, G.; Li, X. Modification by simultaneously γ-WO_3/Li_2WO_4 composite coating and spinel-structure formation on Li $[Li_{0.2}Mn_{0.54}Ni_{0.13}Co_{0.13}]O_2$ cathode via a simple wet process. *J. Alloys Compd.* **2019**, *790*, 421−432.
(32) Reed, J.; Ceder, G.; Van Der Ven, A. Layered-to-spinel phase transition in Li_xMnO_2. *Electrochem. Solid State Lett.* **2001**, *4* (6), A78.
(33) Zhang, H.; Karki, K.; Huang, Y.; Whittingham, M. S.; Stach, E. A.; Zhou, G. Atomic insight into the layered/spinel phase transformation in charged $LiNi_{0.80}Co_{0.15}Al_{0.05}O_2$ cathode particles. *J. Phys. Chem. C* **2017**, *121* (3), 1421−1430.
(34) Jhu, C.-Y.; Wang, Y.-W.; Wen, C.-Y.; Shu, C.-M. Thermal runaway potential of $LiCoO_2$ and Li $(Ni_{1/3}Co_{1/3}Mn_{1/3})O_2$ batteries determined with adiabatic calorimetry methodology. *Appl. Energy* **2012**, *100*, 127−131.
(35) Zhang, H.; Liu, H.; Piper, L. F.; Whittingham, M. S.; Zhou, G. Oxygen Loss in Layered Oxide Cathodes for Li-Ion Batteries: Mechanisms, Effects, and Mitigation. *Chem. Rev.* **2022**, *122* (6), 5641−5681.
(36) Lu, X.; Zhao, L.; He, X.; Xiao, R.; Gu, L.; Hu, Y.-S.; Li, H.; Wang, Z.; Duan, X.; Chen, L.; Maier, J.; Ikuhara, Y. Lithium storage in $Li_4Ti_5O_{12}$ spinel: the full static picture from electron microscopy. *Adv. Mater.* **2012**, *24* (24), 3233−3238.
(37) Shen, L.; Uchaker, E.; Zhang, X.; Cao, G. Hydrogenated $Li_4Ti_5O_{12}$ nanowire arrays for high rate lithium ion batteries. *Adv. Mater.* **2012**, *24* (48), 6502−6506.
(38) Zhang, W.; Seo, D.-H.; Chen, T.; Wu, L.; Topsakal, M.; Zhu, Y.; Lu, D.; Ceder, G.; Wang, F. Kinetic pathways of ionic transport in fast-charging lithium titanate. *Science* **2020**, *367* (6481), 1030−1034.
(39) Thackeray, M. M.; Amine, K. $Li_4Ti_5O_{12}$ spinel anodes. *Nat. Energy* **2021**, *6* (6), 683−683.
(40) Du, Y.; Kim, D. J.; Kaspar, T. C.; Chamberlin, S. E.; Lyubinetsky, I.; Chambers, S. A. In-situ imaging of the nucleation and growth of epitaxial anatase TiO_2 (001) films on $SrTiO_3$ (001). *Surf. Sci.* **2012**, *606* (17−18), 1443−1449.
(41) Kneiß, M.; Jenderka, M.; Brachwitz, K.; Lorenz, M.; Grundmann, M. Modeling the electrical transport in epitaxial undoped and Ni-, Cr-, and W-doped TiO_2 anatase thin films. *Appl. Phys. Lett.* **2014**, *105* (6), 062103.
(42) Breeson, A. C.; Sankar, G.; Goh, G. K. L.; Palgrave, R. G. Rutile to anatase phase transition induced by N doping in highly oriented TiO_2 films. *Phys. Chem. Chem. Phys.* **2016**, *18* (35), 24722−24728.
(43) Spahr, M. E.; Novák, P.; Schnyder, B.; Haas, O.; Nesper, R. Characterization of layered lithium nickel manganese oxides synthesized by a novel oxidative coprecipitation method and their electrochemical performance as lithium insertion electrode materials. *J. Electrochem. Soc.* **1998**, *145* (4), 1113.
(44) Mesoraca, S.; Kleibeuker, J.; Prasad, B.; MacManus-Driscoll, J.; Blamire, M. Lithium outdiffusion in $LiTi_2O_4$ thin films grown by pulsed laser deposition. *J. Cryst. Growth* **2016**, *454*, 134−138.
(45) Lippens, P.-E.; Womes, M.; Kubiak, P.; Jumas, J.-C.; Olivier-Fourcade, J. Electronic structure of the spinel $Li_4Ti_5O_{12}$ studied by ab initio calculations and X-ray absorption spectroscopy. *Solid State Sci.* **2004**, *6* (2), 161−166.
(46) Thakur, H.; Thakur, P.; Kumar, R.; Brookes, N.; Sharma, K.; Singh, A. P.; Kumar, Y.; Gautam, S.; Chae, K. Irradiation induced ferromagnetism at room temperature in TiO_2 thin films: X-ray magnetic circular dichroism characterizations. *Appl. Phys. Lett.* **2011**, *98* (19), 192512.
(47) Maleknia, S.; Brodbelt, J.; Pope, K. Characterization of the reactive and dissociative behavior of transition metal oxide cluster ions in the gas phase. *J. Am. Soc. Mass Spectrom.* **1991**, *2* (3), 212−219.
(48) Kim, Y. K.; Rousseau, R.; Kay, B. D.; White, J.; Dohnálek, Z. Catalytic dehydration of 2-propanol on $(WO_3)_3$ clusters on TiO_2 (110). *J. Am. Chem. Soc.* **2008**, *130* (15), 5059−5061.
(49) Zhai, H.-J.; Wang, L.-S. Probing the electronic structure of early transition metal oxide clusters: Molecular models towards mechanistic insights into oxide surfaces and catalysis. *Chem. Phys. Lett.* **2010**, *500* (4−6), 185−195.
(50) Ohta, H.; Kim, S.-W.; Ohta, S.; Koumoto, K.; Hirano, M.; Hosono, H. Reactive Solid-Phase Epitaxial Growth of Na_xCoO_2 ($x \sim 0.83$) via Lateral Diffusion of Na into a Cobalt Oxide Epitaxial Layer. *Cryst. Growth Des.* **2005**, *5* (1), 25−28.
(51) Ohta, H.; Mizutani, A.; Sugiura, K.; Hirano, M.; Hosono, H.; Koumoto, K. Surface modification of glass substrates for oxide heteroepitaxy: Pasteable three-dimensionally oriented layered oxide thin films. *Adv. Mater.* **2006**, *18* (13), 1649−1652.
(52) Li, N.; Katase, T.; Zhu, Y.; Matsumoto, T.; Umemura, T.; Ikuhara, Y.; Ohta, H. Solid−liquid phase epitaxial growth of $Li_4Ti_5O_{12}$ thin film. *Appl. Phys. Express* **2016**, *9* (12), 125501.
(53) Katayama, S.; Katase, T.; Tohei, T.; Feng, B.; Ikuhara, Y.; Ohta, H. Reactive Solid-Phase Epitaxy and Electrical Conductivity of Layered Sodium Manganese Oxide Films. *Crys. Growth Des.* **2017**, *17* (4), 1849−1853.
(54) Rawlence, M.; Garbayo, I.; Buecheler, S.; Rupp, J. On the chemical stability of post-lithiated garnet Al-stabilized $Li_7La_3Zr_2O_{12}$ solid state electrolyte thin films. *Nanoscale* **2016**, *8* (31), 14746−14753.

https://doi.org/10.1021/acs.nanolett.2c01701
Nano Lett. 2022, 22, 5530−5537